RESEARCH ARTICLES

QUANTUM INFORMATION

Unconditional quantum teleportation between distant solid-state quantum bits

W. Pfaff,[1*] B. J. Hensen,[1] H. Bernien,[1] S. B. van Dam,[1] M. S. Blok,[1] T. H. Taminiau,[1] M. J. Tiggelman,[1] R. N. Schouten,[1] M. Markham,[2] D. J. Twitchen,[2] R. Hanson[1†]

Realizing robust quantum information transfer between long-lived qubit registers is a key challenge for quantum information science and technology. Here we demonstrate unconditional teleportation of arbitrary quantum states between diamond spin qubits separated by 3 meters. We prepare the teleporter through photon-mediated heralded entanglement between two distant electron spins and subsequently encode the source qubit in a single nuclear spin. By realizing a fully deterministic Bell-state measurement combined with real-time feed-forward, quantum teleportation is achieved upon each attempt with an average state fidelity exceeding the classical limit. These results establish diamond spin qubits as a prime candidate for the realization of quantum networks for quantum communication and network-based quantum computing.

The reliable transmission of quantum states between remote locations is a major open challenge in quantum science. Quantum state transfer between nodes containing long-lived qubits (*1*–*3*) can extend quantum key distribution to long distances (*4*), enable blind quantum computing in the cloud (*5*), and serve as a critical primitive for a future quantum network (*6*). When provided with a single copy of an unknown quantum state, directly sending the state in a carrier such as a photon is unreliable due to inevitable losses. Creating and sending several copies of the state to counteract such transmission losses is impossible by the no-cloning theorem (*7*). Nevertheless, quantum information can be faithfully transmitted over arbitrary distances through quantum teleportation provided the network parties (named "Alice" and "Bob") have previously established a shared entangled state and can communicate classically (*8*–*11*).

[1]Kavli Institute of Nanoscience Delft, Delft University of Technology, Post Office Box 5046, 2600 GA Delft, Netherlands. [2]Element Six, Ltd., Kings Ride Park, Ascot, Berkshire SL5 8BP, UK.
*Present address: Department of Applied Physics, Yale University, New Haven, CT 06511, USA. †Corresponding author. E-mail: r.hanson@tudelft.nl

Unconditional quantum teleportation

In the teleportation protocol (Fig. 1A), Alice is initially in possession of the state to be teleported (qubit 1), which is most generally given by $|\psi\rangle = \alpha|0\rangle + \beta|1\rangle$. Alice and Bob each have one qubit of an entangled pair (qubits 2 and 3) in the joint state $|\Psi^-\rangle_{23} = (|01\rangle_{23} - |10\rangle_{23})/\sqrt{2}$. The combined state of all three qubits can be rewritten as

$$|\psi_1\rangle|\Psi^-\rangle_{23} = \frac{1}{2}[|\Phi^+\rangle_{12}(\alpha|1\rangle_3 - \beta|0\rangle_3) + |\Phi^-\rangle_{12}(\alpha|1\rangle_3 + \beta|0\rangle_3) + |\Psi^+\rangle_{12}(-\alpha|0\rangle_3 + \beta|1\rangle_3) - |\Psi^-\rangle_{12}(\alpha|0\rangle_3 + \beta|1\rangle_3)]$$

where $|\Phi^\pm\rangle = (|00\rangle \pm |11\rangle)/\sqrt{2}$, $|\Psi^\pm\rangle = (|01\rangle \pm |10\rangle)/\sqrt{2}$ are the four Bell states. To teleport the quantum state, Alice performs a joint measurement on her qubits (qubits 1 and 2) in the Bell basis, projecting Bob's qubit into a state that is equal to $|\psi\rangle$ up to a unitary operation that depends on the outcome of Alice's measurement. Alice sends the outcome via a classical communication channel to Bob, who can then recover the original state by applying the corresponding local transformation.

Because the source qubit state always disappears on Alice's side, it is irrevocably lost whenever the protocol fails. Therefore, to ensure that each qubit state inserted into the teleporter unconditionally reappears on Bob's side, Alice must be able to distinguish between all four Bell states in a single shot, and Bob has to preserve the coherence of the target qubit during the communication of the outcome and the final conditional transformation. Several pioneering experiments have explored teleportation between remote nodes (*12*–*14*), but unconditional teleportation between long-lived qubits (*1*–*3*) has so far only been demonstrated within a local qubit register (*15*–*17*).

We demonstrate unconditional teleportation between diamond spin qubits residing in independent setups separated by 3 m. This result is

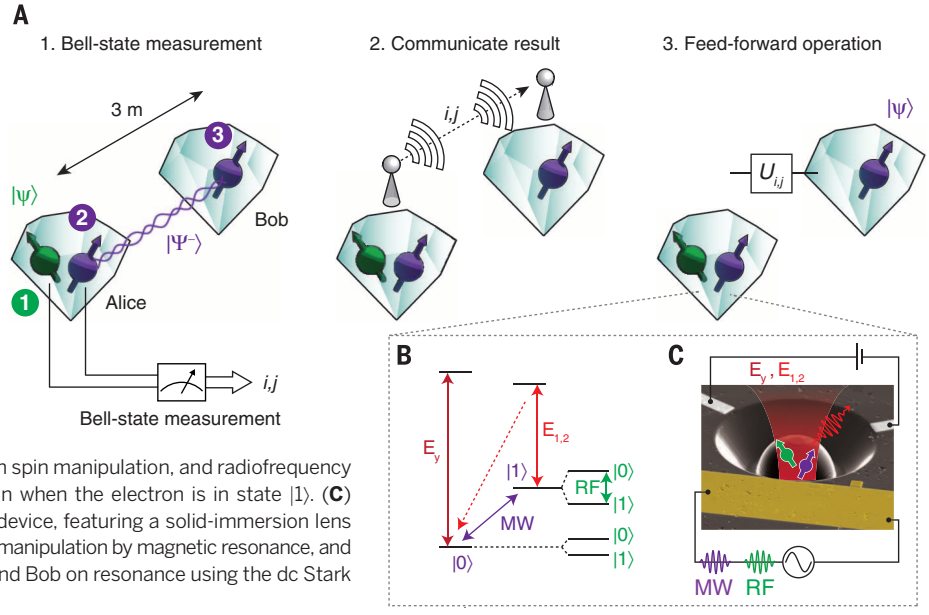

Fig. 1. Teleportation scheme and system description. (**A**) General scheme for teleportation. In our experiment, Alice and Bob each control a single NV center in a single-crystal chemical vapor deposition–grown diamond by operating an independent cryogenic confocal microscope setup (T = 8 K for Alice and T = 4 K for Bob). (**B**) Energy-level scheme and qubit control methods. The source state is encoded in Alice's nitrogen-14 spin (green) with basis states $|0\rangle \equiv m_I = 0$, $|1\rangle \equiv m_I = -1$. Two distant NV electronic spins (purple), with basis states encoded as $|0\rangle \equiv m_s = 0, |1\rangle \equiv m_s = -1$, form the remote entangled pair shared by Alice and Bob. The electron spin is initialized by optical spin pumping on the NV center's $E_{1,2}$ transitions (bright red arrows), and read out by spin-selective optical excitation via the E_y transition (dark red arrow) (*18*). Microwave (MW) pulses allow for electron spin manipulation, and radiofrequency (RF) pulses are used to manipulate the nuclear spin when the electron is in state $|1\rangle$. (**C**) Scanning electron microscope image of a diamond device, featuring a solid-immersion lens for enhanced collection efficiency, a stripline for spin manipulation by magnetic resonance, and electrodes for bringing the optical transitions of Alice and Bob on resonance using the dc Stark effect. See supplementary methods for details (*23*).

achieved by fully separating the generation of remote entanglement (the preparation of the teleporter) from the two-qubit Bell state measurement and feed-forward (the actual teleportation action). In particular, a photonic channel is used to generate heralded remote entanglement between two nitrogen-vacancy (NV) center electronic spins, whereas the teleportation protocol solely exploits matter qubits that—unlike photonic qubits—allow for a deterministic Bell state measurement with current technology. The source state is encoded in a nuclear spin close to one of the NV electron spins after preparation of the teleporter. We preserve the target qubit's coherence by dynamical decoupling while the measurement outcome is forwarded and the final correction pulse is applied. This protocol ensures that the source state is successfully teleported in each of the experimental runs.

Experimental implementation: Preparing the teleporter

Alice and Bob each operate an independent low-temperature confocal microscope setup that addresses a single NV center. The two NV electronic spins (labeled as qubits 2 and 3) are used as the distributed entangled pair that is the medium for teleportation. These spins can be initialized and read out in a single shot by spin-resolved optical excitation (*18*) and coherently manipulated using microwave (MW) pulses (*19*) (Fig. 1B).

To prepare the teleporter, the electrons are initialized in the nonlocal entangled state $|\Psi^-\rangle_{23} = (|01\rangle_{23} - |10\rangle_{23})/\sqrt{2}$ through a recently demonstrated protocol (*20*, *21*) that is based on local entanglement between electron spin and photon number and subsequent joint measurement of the photons (Fig. 2A). Because successful entanglement generation is heralded by photon detection events, the protocol is robust against photon loss. Compared to the initial demonstration of this entangling protocol (*21*), we have further enhanced the efficiency of photon collection from our device through an antireflection coating. Also, we have improved both the spectral stability of the NV center's optical transition and the charge state initialization by resonant repumping on the neutral-charge state zero-phonon line (*22*, *23*). As a result, the generation rate of the entangled state $|\Psi^-\rangle_{23}$ is increased fivefold to 1/250 s^{-1} and the entangled state fidelity is improved from 0.73 to an estimated 0.87.

The additional qubit in Alice's node—essential for making the teleportation unconditional—is provided by the nitrogen-14 nuclear spin of Alice's NV (qubit 1). Before establishing the entanglement link, this nuclear spin is initialized into state $|1\rangle$ by a projective measurement via the electron spin (*18*, *24*). We reinitialize the nuclear spin after each 250 entanglement attempts in order to preserve its purity (*23*) (Fig. 2, C and D). The source state is prepared after establishing remote entanglement, thus avoiding possible dephasing of the source state by repeated optical excitation of the nearby electron (*25*, *26*) during entanglement generation. We use a decoherence-protected gate (*27*) on Alice's side to set the nuclear spin to the source state $|\psi\rangle = \alpha|0\rangle + \beta|1\rangle$. This gate combines two nuclear spin rotations with a refocusing pulse on the electron spin such that the entangled state is efficiently preserved for the duration of the gate (Fig. 3, A and B). This operation concludes the preparation of the teleporter and the insertion of the source qubit, with the three-qubit system left in the state $|\psi\rangle_1|\Psi^-\rangle_{23} = (\alpha|0\rangle_1 + \beta|1\rangle_1)(|01\rangle_{23} - |10\rangle_{23})/\sqrt{2}$ (*23*).

Experimental implementation: Teleportation

At the heart of unconditional qubit teleportation is a deterministic Bell-state measurement (BSM) by Alice on qubits 1 and 2 that generally involves two steps. First, the four Bell states are mapped onto the four different qubit eigenstates $|i\rangle_1|j\rangle_2$ by quantum gate operations. In the second step, each of the two qubits is read out in a single shot, and the two measurement outcomes are sent to Bob. In our scheme (Fig. 3, A and B), we implement the Bell-state mapping by applying a two-qubit controlled-NOT gate (CNOT) followed by a $\pi/2$ rotation on the nuclear spin using another decoherence-protected gate (*23*). Then we read out the electron spin in a single shot (average fidelity 0.963 ± 0.005). Finally, we read out the nuclear

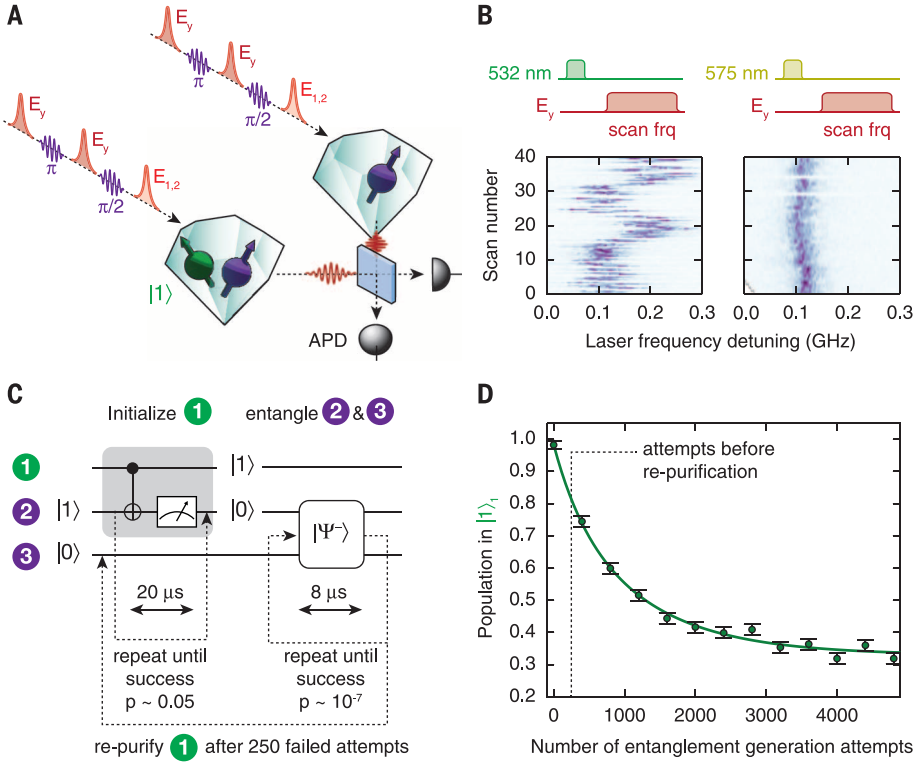

Fig. 2. Preparation of the teleporter. (**A**) Schematic showing generation of remote entanglement. After initializing qubit 1 in $|1\rangle$, the following sequence is applied. First, both qubits 2 and 3 are initialized in $|0\rangle$ by optical pumping. Then a combination of spin rotations and spin-selective optical excitation on E_y creates local entanglement between spin and photon number at each node, followed by two-photon quantum interference and photon detection (for projecting qubits 2 and 3 onto an entangled state) using avalanche photo detectors (APDs) (*20*, *21*, *23*). This sequence is repeated until successful. In the experiment, the photons are guided through fibers to the beamsplitter and the APDs. (**B**) Measurement of the frequency stability of the optical transition labeled E_y. We repeatedly apply a charge repump pulse and then scan a red laser (5 nW) over the E_y resonance. Spectral diffusion is strongly slowed down for the charge repump laser (50 nW) on resonance with the NV^0 zero-phonon line at 575 nm (right) compared to conventional off-resonant charge repumping using laser light (150 µW) at 532 nm (left) (*22*). For the scans using a 575-nm repump laser, we apply a strong laser pulse on resonance with NV^- (50 nW) before each scan to enforce ionization to NV^0. The red laser frequency shown is relative to 470.4636 THz. Color encodes the photon count rate during the scan; darker color indicates higher intensity. (**C**) Circuit diagram for the periodic measurement-based reinitialization of the nuclear spin (qubit 1) in between remote entanglement-generation attempts. Both the probability for success per attempt and the time duration of a single attempt are indicated for the initialization by measurement of qubit 1 and the generation of entanglement between qubits 2 and 3. (**D**) Measured probability $P(|1\rangle)$ to preserve the initialized nuclear spin state $|1\rangle$ as a function of number of entanglement generation attempts N_{ent}. A fit (solid line) to a rate-equations model yields a probability of $(0.85 \pm 0.05) \times 10^{-3}$ per entanglement-generation attempt that the nuclear spin flips (*23*). The dashed line marks the maximum number of attempts before the nuclear spin is reinitialized ($N_{ent} = 250$).

spin by mapping its state onto the electron spin, followed by electron spin readout. The two single-shot readout results give the outcome of the BSM.

We benchmark the BSM by preparing each of the four Bell states as input states in Alice's register (Fig. 3C). This procedure yields an uncorrected mean fidelity, given by the probability to obtain the measurement result corresponding to the prepared Bell state, of 0.89 ± 0.02. To gain more insight into the sources of imperfections, we compare the data with numerical simulations that use the independently determined infidelities of the nuclear spin initialization, CNOT gate, and electron single-shot readout as input. These simulations predict an average fidelity of 0.9 (Fig. 3C) (*23*), in excellent agreement with the data. Taking known errors in the preparation of the input states into account, we infer a BSM fidelity of 0.93 ± 0.02.

The final challenge for successful unconditional teleportation is to maintain the coherence of Bob's target qubit (qubit 3) during the BSM and feed-forward. In our experiment, Bob's qubit is mostly affected by interactions with the surrounding nuclear spin bath. We counteract this

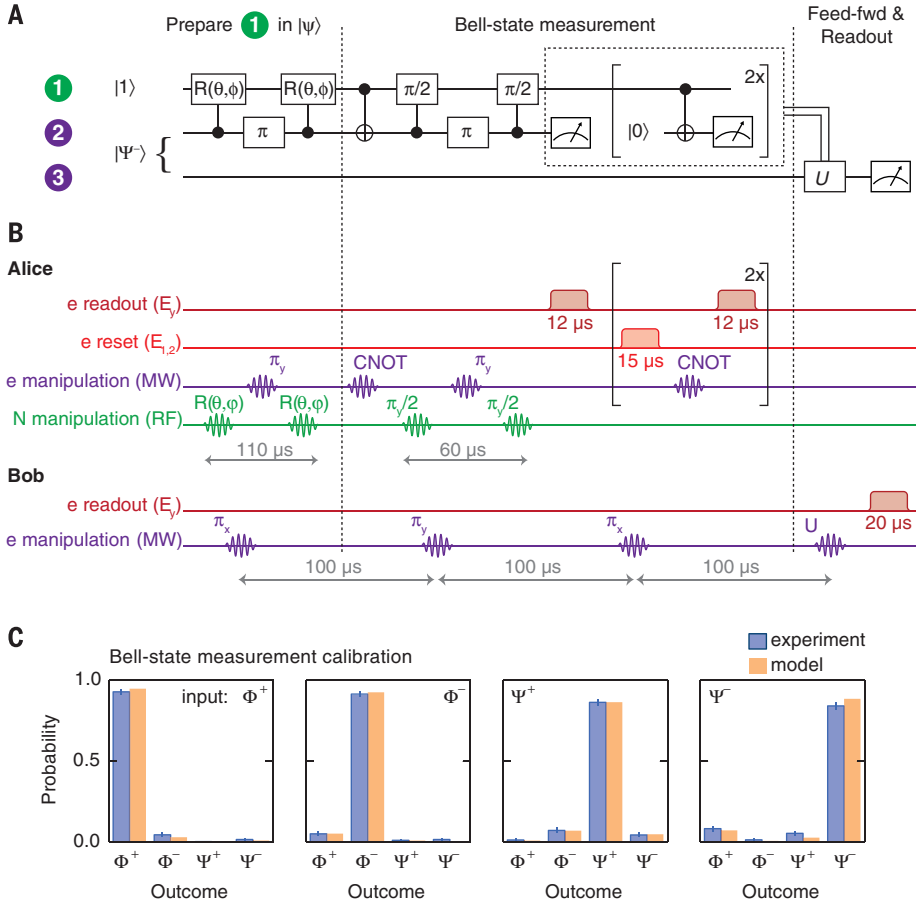

Fig. 3. Deterministic Bell-state measurement (BSM) and real-time feed-forward. (**A**) Circuit diagram and (**B**) pulse scheme of our implementation. The label "e" ("N") indicates operations acting on the electron spin (nitrogen nuclear spin). To enhance the readout fidelity for the nuclear spin, we perform the mapping to the electron spin via a CNOT and the subsequent electron readout twice. While Alice is performing her BSM, Bob applies an XY4 decoupling sequence on his electron qubit. After receiving the BSM outcome from Alice, Bob applies the feed-forward operation U and reads out his qubit. $\pi_{x,y}$ denote rotations around the x axis and y axis, respectively. (**C**) Characterization of the BSM by inserting the four different Bell states on Alice's side and determining the probability with which the ideal outcome is observed (blue bars). Data are not corrected for imperfect preparation of the input states. Expectations based on independently determined experimental imperfections are shown in orange. Error bars are two statistical SDs.

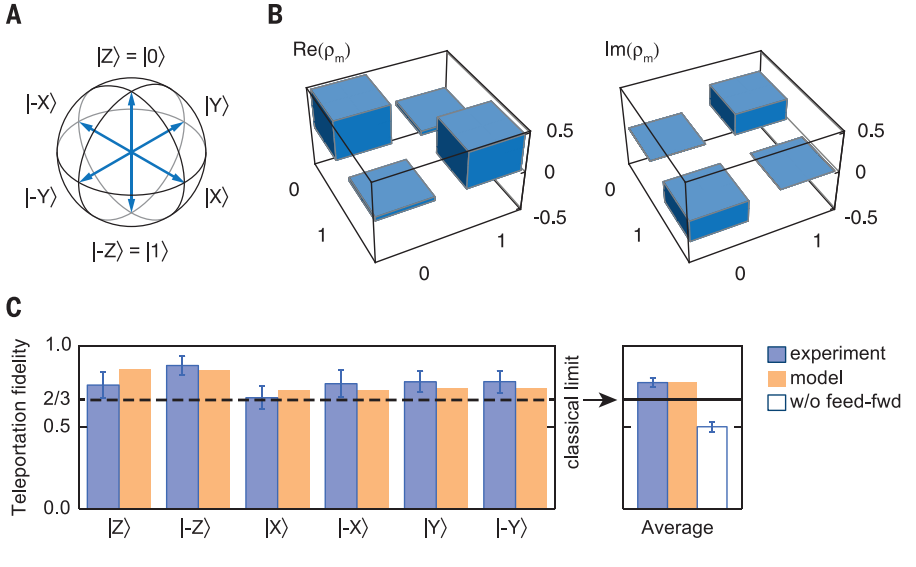

Fig. 4. Demonstration of unconditional quantum teleportation between remote qubits. (**A**) Bloch sphere with the six mutually unbiased basis states that we teleport. $|\pm X\rangle = (|0\rangle \pm |1\rangle)/\sqrt{2}$, $|\pm Y\rangle = (|0\rangle \pm i|1\rangle)/\sqrt{2}$. (**B**) State tomography after teleportation of the input state $|Y\rangle$. We determine the density matrix ρ_m by measuring the expectation values of the Pauli spin operators, $\langle\sigma_x\rangle$, $\langle\sigma_y\rangle$, $\langle\sigma_z\rangle$, where the required qubit rotations before readout are performed conditional on the BSM outcome. The measured (ideal) entries of the density matrix are $\rho_{00} = 1 - \rho_{11} = 0.52 \pm 0.08$ (0.5) and $\rho_{01} = (\rho_{10})^* = [0.05 \pm 0.08] - i[0.28 \pm 0.07]$ ($-i0.5$), respectively. (**C**) Average teleportation fidelity from the measured fidelities of the six states (blue bars). Sample sizes are (left to right) 54, 89, 73, 49, 52, and 47. Predictions from simulations are shown in orange. Without feed-forward, the target state is completely mixed (white bar). The horizontal line marks the classical limit of 2/3 (*30*). Data are not corrected for source state initialization errors. Uncertainties are 1 statistical SD.

decoherence by applying an XY4 dynamical decoupling sequence (*19*, *28*, *29*). The time between entanglement generation and the triggering of the feed-forward operation based on the BSM outcome is 300 μs. For this duration, the decoupling protocol preserves the qubit state, with an average fidelity of 0.96 ± 0.02.

Verifying quantum teleportation

We first verify that the teleporter is calibrated correctly by applying it to the nominal input state $|Y\rangle = (|0\rangle + i|1\rangle)/\sqrt{2}$ and performing tomography on the state that appears on Bob's side. The reconstructed density matrix (Fig. 4B) shows that the target state vector is aligned well with Y and therefore that the reference frames of Alice and Bob are correctly set.

To prove that our quantum teleporter outperforms any classical communication strategy, we teleport an unbiased set of six basis states $|\psi\rangle$ (Fig. 4A) and determine the fidelity of the teleported state on Bob's side with respect to the ideal input state. In these experiments, we use a feed-forward operation that maps the ideal state of qubit 3 onto a qubit eigenstate such that the readout directly yields the teleportation fidelity (*23*). Because the feed-forward operation is conditional on the BSM outcome, ignoring the BSM outcome yields a completely mixed state and random outcomes, ensuring that no information is transmitted. Without feed-forward, we indeed observe a mean teleportation fidelity, averaged over all six input states, of $\langle F\rangle = 0.50 \pm 0.03$ (Fig. 4C). In contrast, including the feed-forward loop, we find that $\langle F\rangle = 0.77 \pm 0.03$. This value exceeds the classical limit of 2/3 by more than 3 standard deviations, thus proving the quantum nature of our teleporter (*30*). We note that this fidelity presents a lower bound on the actual teleportation fidelity because it does not take into account initialization errors of the source state. Notably, this result is obtained without any postselection: Each teleportation attempt is included in the data presented here.

We also simulate the outcomes by using independently determined infidelities in the protocol. The only unknown parameter is the fidelity of the entangled state shared by Alice and Bob. We find that our data are well reproduced by the simulations if we assume a fidelity to the ideal Bell state $|\Psi^-\rangle_{23}$ of 0.87 (Fig. 4C). The simulations also enable us to quantify the effect of imperfect initialization of the source qubit on the measured fidelities. In this way, we estimate the teleportation fidelity to be ~0.86 (*23*).

Conclusions and outlook

The ability to generate remote entanglement and to control and read out multiple qubits per node, as shown in the present teleportation experiment, makes NV centers a leading candidate for realizing a quantum network (*6*, *31*). Our teleportation scheme is both unconditional and scalable to large distances, as it can mitigate photon loss by heralding and purification of the distributed entangled state (*4*). Our current capabilities could be supplemented with quantum memories that are robust against optical excitation of the electrons, enabling remote entanglement purification (*4*, *32*) and the connection of multiple nodes into the network. A promising route is the use of weakly coupled nuclear spins (*33*–*35*) on which multi-qubit quantum control has very recently been demonstrated (*36*). For such nuclear spins, coherence times of >1 s under optical excitation have been reported (*37*), while the incorporation of NV centers into optical cavities may enable remote entanglement generation on millisecond time scales (*38*). Furthermore, the entanglement and readout fidelities reported here are sufficient for a violation of a Bell inequality with the detection loophole closed, making NV centers a promising system for realizing a loophole-free Bell test and device-independent quantum key distribution (*39*).

REFERENCES AND NOTES

1. D. D. Awschalom, L. C. Bassett, A. S. Dzurak, E. L. Hu, J. R. Petta, *Science* **339**, 1174–1179 (2013).
2. M. H. Devoret, R. J. Schoelkopf, *Science* **339**, 1169–1174 (2013).
3. C. Monroe, J. Kim, *Science* **339**, 1164–1169 (2013).
4. H. J. Briegel, W. Dür, J. I. Cirac, P. Zoller, *Phys. Rev. Lett.* **81**, 5932–5935 (1998).
5. S. Barz *et al.*, *Science* **335**, 303–308 (2012).
6. H. J. Kimble, *Nature* **453**, 1023–1030 (2008).
7. W. K. Wootters, W. H. Zurek, *Nature* **299**, 802–803 (1982).
8. C. H. Bennett *et al.*, *Phys. Rev. Lett.* **70**, 1895–1899 (1993).
9. D. Bouwmeester *et al.*, *Nature* **390**, 575–579 (1997).
10. A. Furusawa *et al.*, *Science* **282**, 706–709 (1998).
11. S. Takeda, T. Mizuta, M. Fuwa, P. van Loock, A. Furusawa, *Nature* **500**, 315–318 (2013).
12. S. Olmschenk *et al.*, *Science* **323**, 486–489 (2009).
13. C. Nölleke *et al.*, *Phys. Rev. Lett.* **110**, 140403 (2013).
14. H. Krauter *et al.*, *Nat. Phys.* **9**, 400–404 (2013).
15. M. Riebe *et al.*, *Nature* **429**, 734–737 (2004).
16. M. D. Barrett *et al.*, *Nature* **429**, 737–739 (2004).
17. L. Steffen *et al.*, *Nature* **500**, 319–322 (2013).
18. L. Robledo *et al.*, *Nature* **477**, 574–578 (2011).
19. G. de Lange, Z. H. Wang, D. Ristè, V. V. Dobrovitski, R. Hanson, *Science* **330**, 60–63 (2010).
20. S. D. Barrett, P. Kok, *Phys. Rev. A* **71**, 060310 (2005).
21. H. Bernien *et al.*, *Nature* **497**, 86–90 (2013).
22. P. Siyushev *et al.*, *Phys. Rev. Lett.* **110**, 167402 (2013).
23. Materials and methods are available at *Science* Online.
24. P. Neumann *et al.*, *Science* **329**, 542–544 (2010).
25. L. Jiang *et al.*, *Phys. Rev. Lett.* **100**, 073001 (2008).
26. M. S. Blok *et al.*, *Nat. Phys.* **10**, 189–193 (2014).
27. T. van der Sar *et al.*, *Nature* **484**, 82–86 (2012).
28. C. A. Ryan, J. S. Hodges, D. G. Cory, *Phys. Rev. Lett.* **105**, 200402 (2010).
29. B. Naydenov *et al.*, *Phys. Rev. B* **83**, 081201 (2011).
30. S. Massar, S. Popescu, *Phys. Rev. Lett.* **74**, 1259–1263 (1995).
31. N. H. Nickerson, Y. Li, S. C. Benjamin, *Nat. Commun.* **4**, 1756 (2013).
32. L. Childress, J. M. Taylor, A. S. Sørensen, M. D. Lukin, *Phys. Rev. Lett.* **96**, 070504 (2006).
33. T. H. Taminiau *et al.*, *Phys. Rev. Lett.* **109**, 137602 (2012).
34. S. Kolkowitz, Q. P. Unterreithmeier, S. D. Bennett, M. D. Lukin, *Phys. Rev. Lett.* **109**, 137601 (2012).
35. N. Zhao *et al.*, *Nat. Nanotechnol.* **7**, 657–662 (2012).
36. T. H. Taminiau, J. Cramer, T. van der Sar, V. V. Dobrovitski, R. Hanson, *Nat. Nanotechnol.* **9**, 171–176 (2014).
37. P. C. Maurer *et al.*, *Science* **336**, 1283–1286 (2012).
38. M. Lončar, A. Faraon, *MRS Bull.* **38**, 144–148 (2013).
39. N. Brunner, D. Cavalcanti, S. Pironio, V. Scarani, S. Wehner, *Rev. Mod. Phys.* **86**, 419–478 (2014).

ACKNOWLEDGMENTS

We thank L. Childress, L. DiCarlo, M. Hatridge, J. J. L. Morton, A. Reiserer, L. M. K. Vandersypen, and P. Walther for valuable discussions. We acknowledge support from the Dutch Organization for Fundamental Research on Matter (FOM), the Defense Advanced Research Projects Agency QuASAR program, the European Union DIAMANT and S3NANO programs, a Marie Curie Intra-European Fellowship, and the European Research Council through a Starting Grant.

SUPPLEMENTARY MATERIALS

www.sciencemag.org/content/345/6196/532/suppl/DC1
Materials and Methods
Figs. S1 to S6
Table S1
References (*40*–*44*)

18 March 2014; accepted 19 May 2014
Published online 29 May 2014;
10.1126/science.1253512

CHRONIC PAIN

Decreased motivation during chronic pain requires long-term depression in the nucleus accumbens

Neil Schwartz,[1] Paul Temkin,[1] Sandra Jurado,[1,2] Byung Kook Lim,[1,3] Boris D. Heifets,[1] Jai S. Polepalli,[1] Robert C. Malenka[1]*

Several symptoms associated with chronic pain, including fatigue and depression, are characterized by reduced motivation to initiate or complete goal-directed tasks. However, it is unknown whether maladaptive modifications in neural circuits that regulate motivation occur during chronic pain. Here, we demonstrate that the decreased motivation elicited in mice by two different models of chronic pain requires a galanin receptor 1–triggered depression of excitatory synaptic transmission in indirect pathway nucleus accumbens medium spiny neurons. These results demonstrate a previously unknown pathological adaption in a key node of motivational neural circuitry that is required for one of the major sequela of chronic pain states and syndromes.

Symptoms that profoundly affect the quality of life of patients with chronic pain include fatigue, reductions in pre-pain activities, and depression (*1*–*4*). A common feature of these symptoms is a decrease in the motivation to undertake and to successfully complete goal-directed actions. Although in the setting of acute pain these features may be adaptive by limiting activity during the healing process and reducing the likelihood of future injury by motivating

Editor's Summary

Toward quantum teleportation on demand

Quantum information processing relies on the ability to store, manipulate, and propagate information encoded in quantum states of matter. Doing so, however, may destroy or compromise these delicate quantum states. Pfaff *et al.* present a quantum teleportation protocol that uses two defects in diamond 3 m apart (see the Perspective by Atatüre and Morton). They then map the quantum state of one of the diamond defects onto the other. The work presents a key building block for the successful development of larger quantum networks.

Science, this issue p. 532; see also p. 510